Exposing Digital Image Forgeries by Detecting Discrepancies in Motion Blur

Pravin Kakar, *Student Member, IEEE*, N. Sudha, *Senior Member, IEEE*, and Wee Ser, *Senior Member, IEEE*

***Abstract*—The widespread availability of photo manipulation software has made it unprecedentedly easy to manipulate images for malicious purposes. Image splicing is one such form of tampering. In recent years, researchers have proposed various methods for detecting such splicing. In this paper, we present a novel method of detecting splicing in images, using discrepancies in motion blur. We use motion blur estimation through image gradients in order to detect inconsistencies between the spliced region and the rest of the image. We also develop a new measure to assist in inconsistent region segmentation in images that contain small amounts of motion blur. Experimental results show that our technique provides good segmentation of regions with inconsistent motion blur. We also provide quantitative comparisons with other existing blur-based techniques over a database of images. It is seen that our technique gives significantly better detection results.**

***Index Terms*—Image cepstrum, image forgery detection, motion blur estimation.**

I. Introduction

FAKE and manipulated images have proliferated in today's media-driven society. The power of the visual medium is compelling and so, malicious tampering can have significant impact on people's perception of events. Misleading images are used for introducing psychological bias, sensationalizing news, political propaganda, and propagating urban myths. The image in Fig. 1, taken from [1], is an instance of the latter. This photograph was widely circulated via e-mail, supposedly having been obtained from a camera found in the debris of the World Trade Center buildings after the attacks of September 11, 2001. The approaching aircraft in the background seems to imply that this image was captured mere seconds before the impact. However, this image is clearly fake. There are many clues within this photograph that help decide that it is a hoax. *A priori* knowledge may be employed to prove that this image is unauthentic. For example, geographical knowledge or information about the type of aircraft involved in the attacks can be used to dismiss this image as fake. Even in the absence of such knowledge, as the camera is focused on the person, the aircraft should have appeared blurred in the image, due to its speed. The complete absence of motion blur in this image indicates a possible forgery. On the other hand, if the original image contains motion blur, how can a spliced region that has had motion blur introduced in it be detected? Introducing motion blur into a spliced object, in general, depends on the perception of the person creating the forgery and hence, is unlikely to be completely consistent with the blur in the rest of the image. In this paper, we use this fact to present a solution to this tampering detection problem. Specifically, we address splicing in a motion-blurred region, with the artificial blur introduced in the spliced part similar to the background blur, so that the inconsistency is difficult to perceive visually.

Fig. 1. Forged "Tourist Guy" image allegedly captured on September 11, 2001.

Many techniques have been developed to discover splicing and compositing of images [2]. Statistical analyses [3], [4] and lighting inconsistencies [5], [6] may be used in order to detect image tampering. Other methods involve exploiting certain features of images which are characteristic of the imaging systems, formats, and the environment [7], [8].

Many of these techniques implicitly assume the lack of any postprocessing on the image [9]. With the appearance of sophisticated photo manipulation software, such an assumption is unlikely to hold for most believable forgeries. Therefore, significant research has gone into circumventing postprocessing (such as blurring) of images. Some techniques [10]–[12] use statistics and measures which are robust to blurring. Others [9], [13]–[16] use discrepancies in defocus blur to discover forgeries. We are not aware of any existing work that uses discrepancies in motion blur, although the authors of [13] suggest that their methods can be extended to motion blur as well . We provide a comparison of our results with theirs below.

The key contributions of this paper are:

- an original forgery detection approach employing motion blur estimation via spectral characteristics of image gradients, which can detect small inconsistencies in motion blur;
- a novel blur estimate measure designed especially to deal with very little motion blur;

Manuscript received November 03, 2010; revised February 15, 2011; accepted February 20, 2011. Date of publication February 28, 2011; date of current version May 18, 2011. This work was supported by a Ph.D. scholarship awarded to P. Kakar by the Institute for Media Innovation. The associate editor coordinating the review of this manuscript and approving it for publication was Dr. Oscar C. Au.

The authors are with the Institute for Media Innovation, Nanyang Technological University, Singapore 637553 (e-mail: pkakar@pmail.ntu.edu.sg; sudha@ntu.edu.sg; ewser@ntu.edu.sg).

Color versions of one or more of the figures in this paper are available online at http://ieeexplore.ieee.org.

Digital Object Identifier 10.1109/TMM.2011.2121056

- a no-reference perceptual blur metric extended to directional motion blur;
- a Hausdorff distance-based cost measure for evaluating the efficiency of our technique.

This paper is an extension of our work reported in [17]. We change the motion blur estimation technique from spectral matting to image gradients for faster processing. We refine the segmentation process in order to provide better results and deal with cases of more complex blurs. We develop new measures in order to reduce the amount of human intervention needed in our technique and improve its robustness. We also provide a detailed quantitative analysis of the efficiency of our technique and test our technique on a database of images.

The organization of this paper is as follows. We present an overview of the cause of motion blur in images in Section II-A, background information about the blur estimation process in Section II-B, and our proposed forgery detection method is presented in Section III. Results and comparisons are provided in Section IV.

II. Motion Blur Estimation

A. Overview of Motion Blur

One of the possible causes of motion blur is the slow speed of the camera shutter relative to the object being imaged. In many images, camera shake is found to be the culprit for the presence of motion blur. Reducing the exposure interval of the camera is a possible solution, but this often affects the amount of noise or depth of field adversely. Tripods and flashes also offer solutions to the problem of motion blur by allowing for more stable exposures or greater illumination in a short interval of time, respectively, but these are often impractical. Hence, many images containing motion blur do exist and so, it is useful to utilize the inconsistencies in motion blur in order to detect image tampering.

Motion blur can be artificially created in an image by specifying the magnitude and direction of the desired blur. Although perceptual clues in the image may be used to determine the direction of the blur, the magnitude of the blur is not, in general, based on any such clues, except the perception of uniformity with other parts of the image having the desired motion. Hence, it is likely that a motion-blurred spliced region is not completely consistent with the rest of the image.

We can model motion blur by averaging the instantaneous intensity falling on a pixel over the shutter interval. Such an averaging process can be weighted by a "soft" Gaussian window instead of using the idealized shutter interval, in order to allow for non-ideal mechanical shutter effects. Alternatively, blurs arising from motion, like other types of blur, can also be considered as convolving an in-focus image with a blur kernel in the spatial domain. The motion blur kernel is determined by the relative velocities of the camera and the objects in the image.

However, in general, neither information about the motion nor the sharp image are available, making blind motion estimation a difficult problem. Approaches involving multiple images [18], [19] have been proposed, but may not be suitable for image forensics. Instead of using spectral matting as in [17], we employ image gradients in order to take advantage of their simpler and faster computations

B. Blur Estimation

We use a variant of the widely recognized cepstral method [20]–[22] in order to estimate motion blur. Instead of employing the cepstrum directly, we use the spectral characteristics of the image gradients as proposed in [23]. Such an approach has been shown to be more robust to noise and somewhat non-uniform motion than just using the cepstrum of the image.

For the case of uniform motion blur, the blurring process is modeled as the convolution of a sharp image with a blurring kernel:

$$I(x,y) = (H * P)(x,y) + N(x,y) \tag{1}$$

where I is the blurred image, H is the sharp image, P is the blurring kernel, and N is the noise present. x and y are the pixel coordinates.

For a horizontal uniform velocity motion blur, the blurring kernel P_u can be modeled as $P_u = 1/L[1,1,\ldots,1]_{1\times L}$, where L is the length of the kernel. Note that a directional blurring kernel P_{θ_0} can be formulated by rotating P_u by θ_0 degrees about the x-axis. Taking the Fourier transform of (1)

$$\hat{I} = \hat{H}\hat{P} + \hat{N} \tag{2}$$

where $\hat{X}$ represents the Fourier transform of X. It is observed that

$$\hat{P}_u(\omega) = \frac{\sin(\pi\omega L)}{\pi\omega L} = \operatorname{sinc}(\pi\omega L) \tag{3}$$

which is known to have periodic zeros at $\{\omega = k/L,\ k = \pm1, \pm2, \ldots\}$. These periodic zeros also appear in $\hat{I}$ if $\hat{N}$ is ignored. The blur extent L is estimated from the cepstrum of the image $\mathcal{C}(I)$:

$$\mathcal{C}(I) = \widehat{\log\left|\hat{I}\right|} \tag{4}$$

which has two peaks separated by $2/L$, due to the large periodic negative spikes in $\hat{P}_u$.

The fast decay of the sinc function makes detecting the periodic zero pattern difficult to discern, especially in noisy images. However, a similar periodic pattern that is easier to detect also exists in the blurred image's gradient in the spectral domain. Differentiating (1), we get

$$I' = (H * P)' + N'. \tag{5}$$

Taking the Fourier transform and omitting the noise term

$$\hat{I}'(\omega) = \hat{H}(\omega)\hat{P}'(\omega). \tag{6}$$

Therefore, we obtain

$$\hat{P}'_u = \left|i2\pi\omega\hat{P}_u(\omega)\right| = \frac{2}{L}\left|\sin(\pi\omega L)\right|. \tag{7}$$

As can be seen, this is a non-decaying term and hence, detecting the peaks in this case should be easier. For a blurred image, the distance between the two peaks in $\mathcal{C}(I')$ determines the blur extent and the orientation of the straight line through the two peaks determines the direction of the blur. However, this is often found to be far from ideal due to noise, poor modeling of the blur, the presence of spurious peaks, etc.

So, instead of directly detecting the cepstral peaks, the Radon transform, which is widely used for detecting straight lines in noisy images, is used. For a motion-blurred image, there are periodic large negative lines in $\log\left|\hat{I}'\right|$ with slope θ_0 and periodicity $1/L$. Denoting the Radon transform by $\mathcal{R}$, $\mathcal{R}\left(\log\left|\hat{I}'\right|\right)$ will have periodic peaks located at $(\pm 1/L, 90 - \theta_0^\circ), (\pm 2/L, 90 - \theta_0^\circ), (\pm 3/L, 90 - \theta_0^\circ), \ldots$. Therefore, this should correspond to a peak in the Fourier transform of $\mathcal{R}\left(\log\left|\hat{I}'\right|\right)$. Denoting this Fourier transform of the Radon transform by $\mathcal{F}$, let the peak in $\mathcal{F}\left(\log\left|\hat{I}'\right|\right)$ occur at (ω_0, ψ_0). Then, we have

$$\omega_0 = \frac{1}{L},\ \psi_0 = 90 - \theta_0^\circ. \tag{8}$$

We represent this estimated motion blur as a two-element vector $\phi = \left[\phi^{mag}\ \phi^{dir}\right]$, where $\phi^{mag} = L$ and $\phi^{dir} = \theta_0$.

An issue arises if the original image has multiple motion blurs present. This is often the case when a moving object is imaged against a still background or vice versa. In [24], segmentation of an image into various regions depending on the estimated blur model for each pixel has been proposed. The technique is useful if the original image contains multiple motion blurs. In this case, the blur models could be separated. While this is appropriate for images with significantly different blurs, it is not feasible for image forgeries. As the region spliced into an image is desired to be concealed from detection, the blur added to it is likely to be similar to that of the surrounding region. In such a case, it would be difficult to estimate a separate blur model for the suspected region at a global level. A localized technique is necessary to separate blur models in case of forgeries.

Examples of such multiple motion blur segmentation are shown in Fig. 2. As can be seen, motion blurs which differ from each other to a relatively large extent are clearly segmented using a Markov random field-based energy segmentation technique [25]. However, it is important to note that the spliced region is not segmented due to having a different blur compared to its surrounding region in any of these images. Therefore, such a technique is useful in dealing with cases in which multiple motion blurs are present in the original image itself, but not for detecting the forged region. Each segment can then be analyzed for consistency using our technique described below.

III. Proposed Forgery Detection Technique

We propose a method to detect image forgeries using motion blur estimates. Blur estimates are first computed from the given image, as defined in Section II-B. Our technique then segments the image based on these estimates, giving the regions with inconsistent blur. Although the technique segments such regions in both authentic and forged images, it is especially useful for exposing the possible forgeries in blurred regions, such as spliced objects with artificial blur perceptually close to the background blur, making the inconsistency in blur difficult to detect. A flowchart outlining the steps in our technique is shown in Fig. 3.

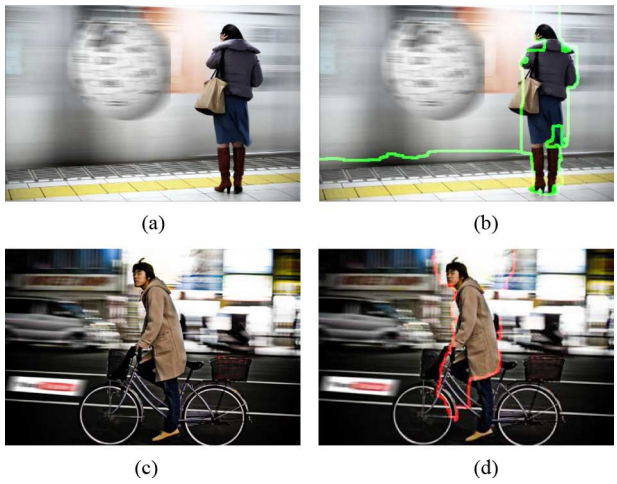

Fig. 2. Multiple motion blur segmentation using Markov random fields [25]. The spliced regions are the Wikipedia and Youtube logos in the top and bottom rows, respectively. Left column: Tampered images with multiple blurs. Right column: Segmentation results.

A. Block-Level Analysis

Given an image having an artificially motion-blurred spliced region, it is not possible to extract multiple blur models over the whole image from its gradients, especially when the blurs are quite similar to each other. Hence, we propose estimating the blur at a local level allowing for different blur models to be estimated, without being lost in noisy data at a global level. The image I is divided into $M_b \times N_b$ overlapping blocks $b_{m,n}$, $m = 1$ to M_b, $n = 1$ to N_b, and the motion blur estimate $\phi_{m,n}$ for each block is calculated. $\phi_{m,n}$ is a two-dimensional vector $\left[\phi_{m,n}^{mag}\ \phi_{m,n}^{dir}\right]$ consisting of the motion blur estimate magnitudes and directions. The image subdivision has two major benefits: 1) Motion blur can be estimated at a number of points, as opposed to just a single estimate for the entire image, giving improved resolution, and 2) space-invariance of motion blur can be assumed over each block, allowing for simpler calculations.

B. Smoothing

The components of the motion blur estimates $\phi_{m,n}$ can be represented in magnitude and direction estimate matrices $\mathbf{\Phi}^{mag}$ and $\mathbf{\Phi}^{dir}$, respectively, each of size $M_b \times N_b$, i.e.,

$$\mathbf{\Phi}^k = \begin{pmatrix} \phi^k_{1,1} & \phi^k_{1,2} & \cdots & \phi^k_{1,N_b} \\ \phi^k_{2,1} & \phi^k_{2,2} & \cdots & \phi^k_{2,N_b} \\ \vdots & \vdots & \ddots & \vdots \\ \phi^k_{M_b,1} & \phi^k_{M_b,2} & \cdots & \phi^k_{M_b,N_b} \end{pmatrix} \quad k = mag, dir. \tag{9}$$

Since $\phi_{m,n}$ is calculated independently for each block $b_{m,n}$, we perform a smoothing operation to correct for small variations in the estimated blurs. We smooth both the magnitudes and the directions of the estimates:

$$\mathbf{\Phi}^k_{smooth} = \mathbf{\Phi}^k * h^k,\ k = mag, dir \tag{10}$$

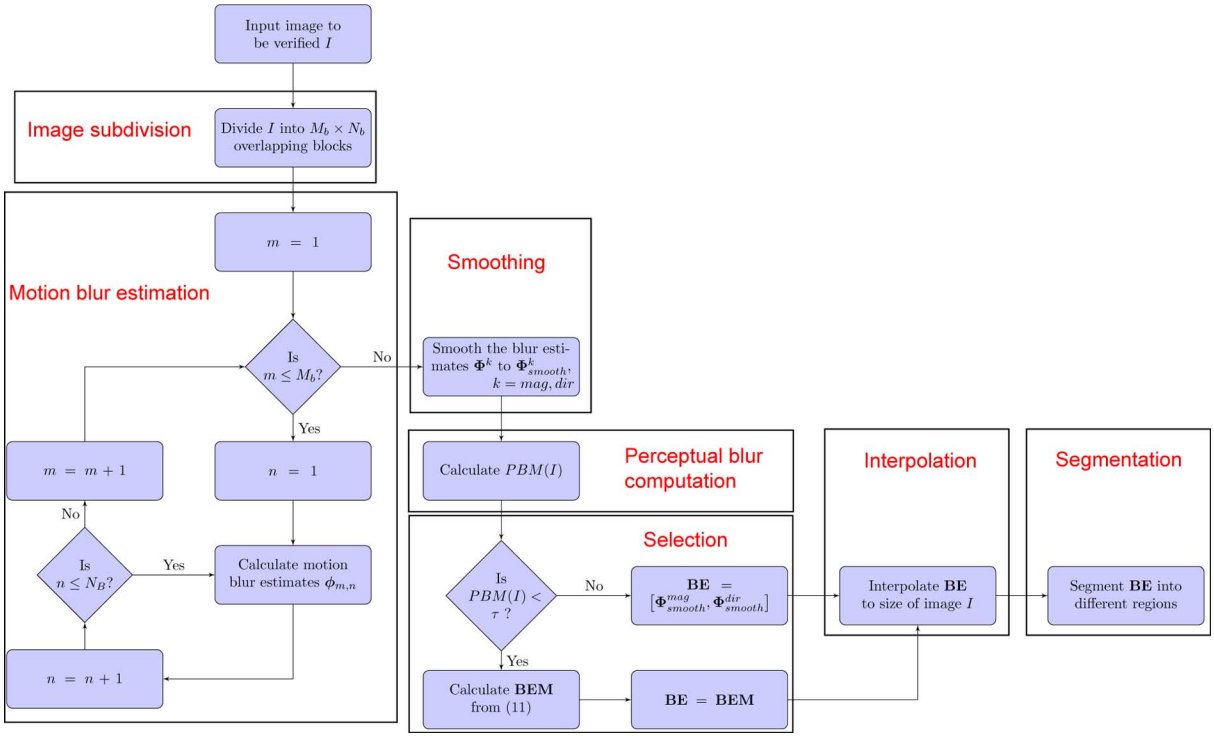

Fig. 3. Flowchart for proposed forgery detection technique.

where $\mathbf{\Phi}^k_{smooth}$ represent the respective smoothed estimates and h is the smoothing filter employed. A disk filter was used in both cases in our technique.

Fig. 4 shows an example for smoothed motion blur estimates. These estimates were obtained for a region containing different motion blurs. As can be seen, the local estimates display some variability at the border between the two regions due to the multiple blurs present in the same block for each local estimate. Smoothing allows the local estimates to vary in a non-abrupt manner, which results in better segmentation of the image in subsequent steps.

C. Blur Estimate Measures

For images in which certain regions appear to have little perceptible motion blur, we propose using the gradients of I along with the motion blur estimates $\mathbf{\Phi}^{mag}_{smooth}$, generating a new *blur estimate measure (BEM)*, in order to improve robustness:

$$BEM(m,n) = \frac{\nabla I \cdot w_{i,j}}{\phi^{mag}_{smooth}(m,n)} \tag{11}$$

where $w_{i,j}$ is a neighborhood window located at the center (i,j), in pixel coordinates, of each block $b_{m,n}$ of the image I and of the same size as the block. As formulated above, (11) can distinguish between the cases where there is little motion blur due to better focusing and where there is a small amount of motion blur due to the lack of enough texture to give significant information about the motion blur present. Only the magnitudes of the motion blur are considered as the direction estimates are perpendicular to the image gradients. Similar to $\mathbf{\Phi}^k$ in (9), $BEM(m,n)$ can be arranged in an $M_b \times N_b$ matrix $\mathbf{BEM}$, as $\phi^k_{m,n}$ and $BEM(m,n)$ are calculated block-wise.

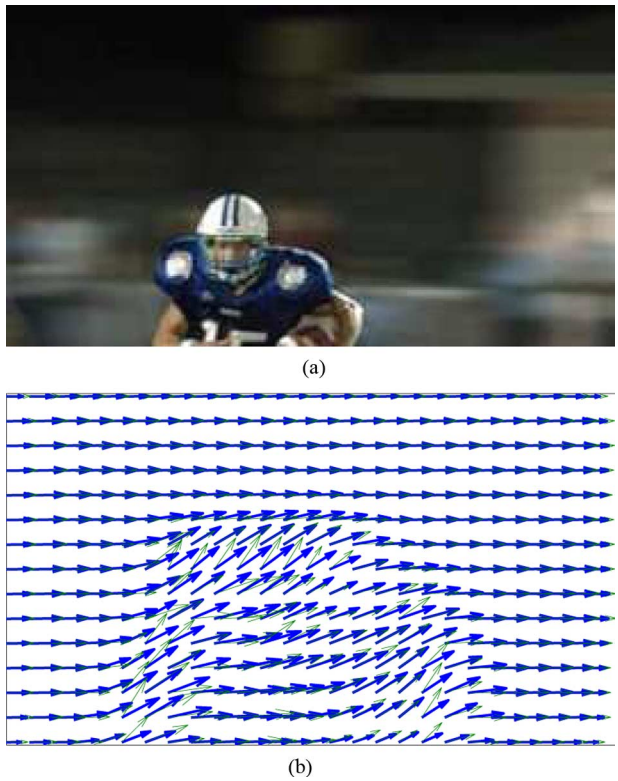

(a)

(b)

Fig. 4. Smoothing motion blur estimates (magnitudes and directions indicated by arrows). (a) Image with consistent motion blur. (b) Smoothing local motion blur estimates. Green regular arrows indicate estimates before smoothing; bold arrows, after smoothing.

In order to automate the decision of using BEMs or just motion estimates, we employ a modification of the no-reference

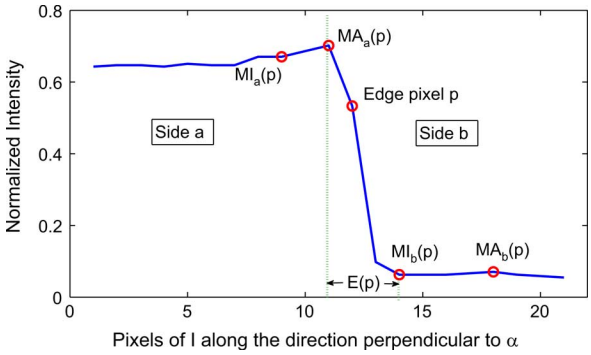

Fig. 5. Computation of edge width $E(p)$.

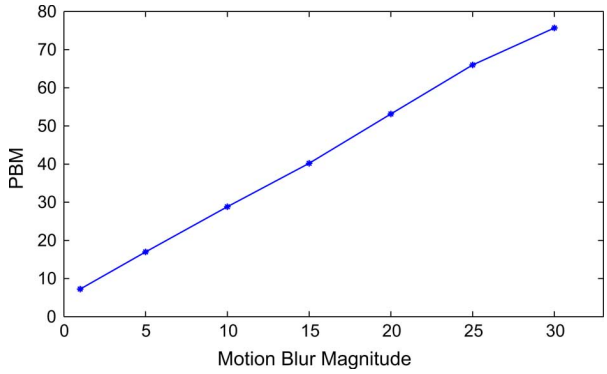

Fig. 6. Blur measurement for motion-blurred images.

perceptual blur metric (PBM) presented in [26]. This metric is intended for Gaussian and compression blurs, necessitating a modification to deal with motion blur, which is not isotropic. Let S_α be the set of edge pixels in the binary edge map of I obtained by applying the Sobel operator in the direction α. A new metric, named as *oriented blur metric* PBM_α, is defined as

$$PBM_\alpha(I) = \frac{\sum_{p \in S_\alpha} E(p)}{|S_\alpha|} \tag{12}$$

where $E(p)$ is the width of the edge along the direction perpendicular to α at the edge pixel p and $|\cdot|$ denotes cardinality.

In order to define $E(p)$ in (12), let the two sides of the line in the direction α at some p be denoted by a and b, as shown in Fig. 5. Also, let the pixel locations of the first local maximum and minimum from this p, along the above perpendicular line, on the side a be denoted by $MA_a(p)$ and $MI_a(p)$, respectively. $MA_b(p)$ and $MI_b(p)$ are defined similarly. Then, we can define the edge width as

$$E(p) = \min(|MA_a(p) - MI_b(p)|, |MA_b(p) - MI_a(p)|). \tag{13}$$

We compute the oriented PBMs for orientations α_i, $i = 1$ to t, where t is the number of orientations evaluated and then define the overall PBM as

$$PBM(I) = \max(PBM_{\alpha_i}) \, \forall \, \alpha_i. \tag{14}$$

This metric is used to determine the overall blurriness of the image as large edge widths, indicating blurred edges, give high values of $PBM(I)$. BEMs are chosen when it is below a predetermined threshold τ. The chosen blur estimate $\mathbf{BE}$ is given by

$$\mathbf{BE} = \begin{cases} \mathbf{BEM}, & \text{if } PBM(I) \leq \tau \\ \left[\mathbf{\Phi}^{mag}_{smooth}, \mathbf{\Phi}^{dir}_{smooth}\right], & \text{otherwise.} \end{cases} \tag{15}$$

It is to be noted that $\mathbf{BE}$ is an $M_b \times N_b \times 2$ matrix in the latter case, as both magnitude and direction estimates are employed. In this case, all subsequent operations are carried out independently on each of the $M_b \times N_b$ component matrices.

The PBM computed for images containing various amounts of motion blur is plotted in the graph shown in Fig. 6. The blur metric was calculated as an average over ten random images containing motion blur with the magnitudes specified in Fig. 6 in random directions. In calculating PBM, we use orientations $\alpha_i = 0°, 45°, 90°$ and $135°$. The almost linear nature of the graph indicates that our metric works well in the case of motion blur.

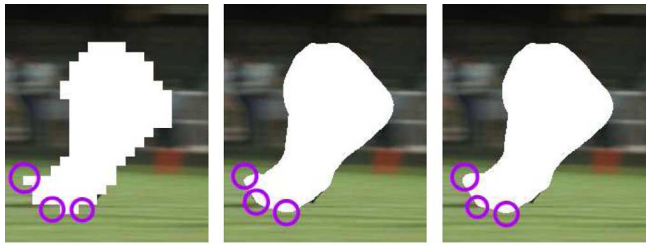

(a) (b) (c)

Fig. 7. Segmentation outputs for various interpolation schemes applied to blur estimates. (a) Nearest neighbor. (b) Bilinear. (c) Bicubic.

D. Interpolation

The motion blur estimates $\mathbf{BE}$ are then upsampled to the size of I using bicubic interpolation, in order to have an estimate of the blur at each pixel. The accuracy of the estimate depends on the amount of upsampling done. Bicubic interpolation provides better results than nearest neighbor (which gives a blocky segmentation) and bilinear interpolation (whose segmentation still has a few jagged edges that could be adequate for certain applications). Fig. 7 shows an example of the segmentation outputs for various interpolations. The circles are examples of regions where the improvement offered by bicubic interpolation over the other two is most clearly visible.

E. Segmentation

We then segment the image into two regions that exhibit different motion blurs. This is done by adaptively thresholding the upsampled $\mathbf{BE}$ using Otsu's method [27]. This method also provides an effectiveness metric which is used to discard images which show consistent directions and/or magnitudes in their motion blur estimates and hence cannot be segmented effectively. The result of segmenting the magnitude and direction of the estimates provides us with an indication of regions with dissimilar motion blur.

The results from this simple segmentation can be refined by again employing an energy-based segmentation. In this case,

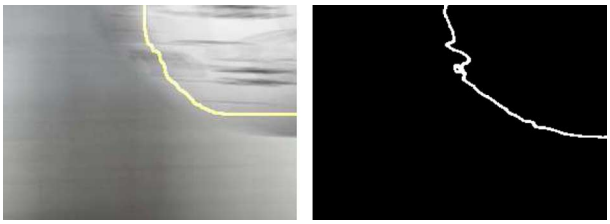

Fig. 8. Left: Energy-based segmentation output. Right: Ideal segmentation obtained by supervised matting.

Fig. 9. Images in our database.

the pixel intensities are considered in addition to the motion blur discrepancies, giving smoother boundaries, more likely to correspond to the actual boundaries of the spliced region. This assumes that the spliced region has a different intensity than its immediate background, which is reasonable. Otherwise, the boundary of the inconsistent region would not be detectable at all, by any method. In order to accomplish such a segmentation, we use the mean values of the motion blur estimates of the two regions obtained by Otsu's method and then find the Euclidean distance between this mean and the motion blur estimate at each pixel. Using graph cuts [28], we find a segmentation which minimizes the total cost consisting of the cost of assigning different adjacent region labels (based on the above Euclidean distance) and the cost of dissimilar neighboring pixel intensities. The results of such a segmentation are shown in Fig. 8.

The ideal segmentation shown in Fig. 8 is obtained by using supervised spectral matting [29] in order to extract the spliced regions from the image and applying Otsu's method to this extracted matte. Obtaining such a segmentation requires knowledge of the spliced region, making it useful only for evaluating splicing detection. Note that the same ideal segmentation can be used for comparison with the energy-based segmentation approach as well, since supervised matting ensures that the extracted region's boundaries correspond very closely with the spliced object's boundaries.

IV. Results and Comparisons

We created a database of 15 forged images, shown in Fig. 9, containing camera shake and motion blur. The original images

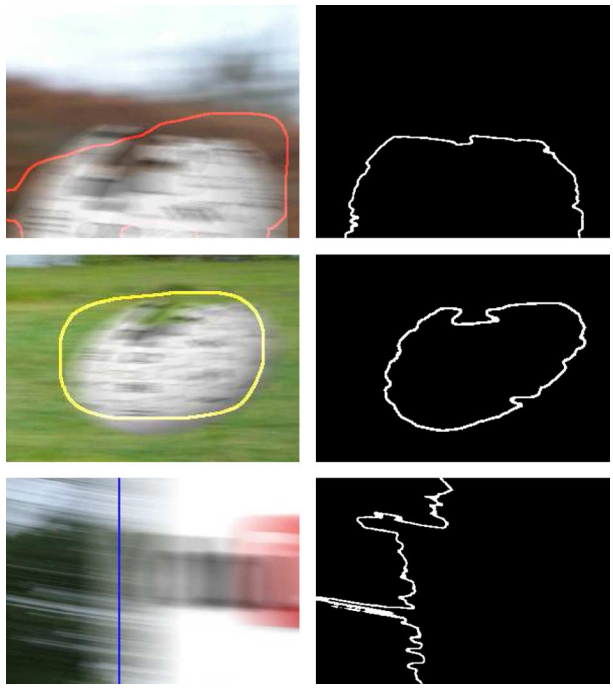

Fig. 10. Detection for spliced blurred regions. Left column: Forged images with segmentation outputs. Right column: Ideal segmentations.

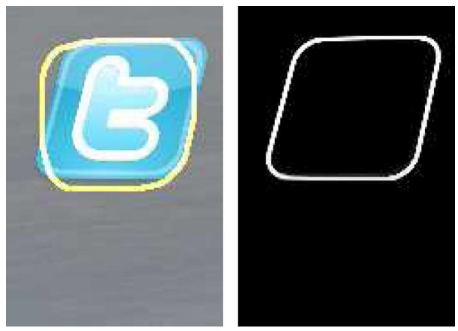

(a) (b)

Fig. 11. Detection for non-blurred spliced region. (a) Segmentation of image with non-blurred spliced object. (b) Ideal segmentation.

were obtained from the popular photo-sharing website Flickr [30]. We spliced different objects into the blurred backgrounds of the images and applied visually similar motion blurs, using the GIMP image editor. The results of detection of spliced regions along with the ground truths showing the actual regions (determined by color similarity) for some images are shown in Fig. 10. An example of the detection for a spliced region that is not blurred is shown in Fig. 11.

A. Evaluation Criteria

In order to evaluate the efficacy of our technique and also determine the various parameters used, we employ a cost measure that is used to determine the difference between the observed and the ideal segmentations.

As the energy-based segmentation gives rise to a boundary dividing the image into different regions, a cost measure like the Hausdorff distance measure which is used widely for shape

TABLE I
SEGMENTATION COST FOR DIFFERENT BLOCK SIZE

Block Size	Segmentation Cost ($\times 10^{-3}$)	
	Otsu's Method	Energy-based
80×80	0.9428	0.7668
100×100	0.9344	0.7402
120×120	0.9613	0.806
140×140	0.9137	0.824
160×160	0.9232	0.8657

TABLE II
SEGMENTATION COST FOR DIFFERENT BLOCK OVERLAP

Block Overlap	Segmentation Cost ($\times 10^{-3}$)	
	Otsu's Method	Energy-based
10	1.0613	0.9092
15	1.6423	0.7668
20	1.2121	0.7402
30	0.9344	0.7757
40	0.9137	0.7502

matching [31], [32] is quite suitable. In the case of both the ideal segmentation and the segmentation from Otsu's method, the perimeter of the extracted region is used as the boundary of the segmentation for evaluation purposes. However, the conventional Hausdorff distance measure considers only the maximum distance between two boundaries and is not robust to outliers in the boundaries. Therefore, we use a modified Hausdorff distance measure, D_{22}, defined in [33].

Let $X = \{x_1, x_2, \ldots, x_M\}$ and $R = \{r_1, r_2, \ldots, r_N\}$ be the observed and ideal segmentation boundaries, respectively. Then, the modified Hausdorff distance measure is given by

$$D_{22}(X, R) = \max\{d(X, R), d(R, X)\} \tag{16}$$

where

$$d(A, B) = \frac{1}{|A|} \sum_{a \in A} \min_{b \in B} \|a - b\|$$

and $|\cdot|$ denotes the cardinality of the set, with $\|\cdot\|$ being the Euclidean distance.

B. Results

Table I shows the variation of the segmentation cost with respect to the block size and Table II with respect to the block overlap. We calculate the motion blur estimates for block sizes of 80×80, 100×100, 120×120, 140×140, and 160×160 pixels with overlaps of 10, 15, 20, 30, and 40 pixels. The average cost function is then evaluated over 15 images for each of the 25 possible combinations of block size and overlap and the minimum average cost is noted. It is observed that the segmentation costs are fairly robust to change in these parameters and energy-based segmentation provides more refined results than simply Otsu's method. We choose to use values of parameters corresponding to the lowest costs for either method (shown in the highlighted cells), i.e., a block size of 100×100 and an overlap of 20 pixels.

1) Choice of τ: We observed that BEMs generally provide good results with images having a mean PBM value of 6.8 and a standard deviation of 1.1, while using only motion blur estimates provides good results with a mean PBM value of 31 and a standard deviation of 13.3. We model the probability distributions for the two cases with normal and inverse Gaussian distributions, respectively. The inverse Gaussian distribution (Fig. 12) is employed for the latter case as significant skew towards higher PBM values is observed in this case. We assume that the prior probabilities of better results using BEMs or only motion blur estimates are equal. Thus, based on the results shown in Figs. 6 and 12, we set τ to 10.

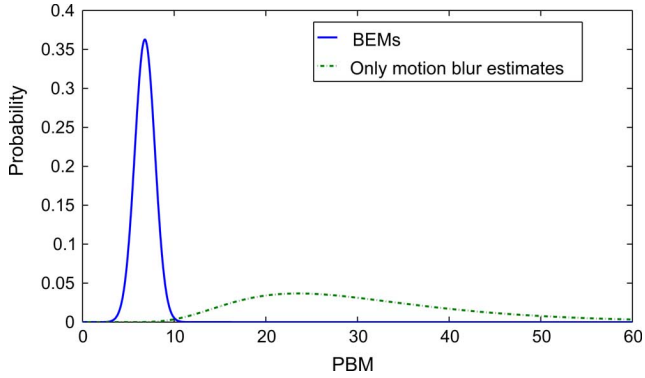

Fig. 12. Probability distributions of PBM values for using BEMs and using only motion blur estimates.

(a) (b)

Fig. 13. Image patches with similar motion blur estimates, but different BEM values. (a) High BEM value. (b) Low BEM value.

2) BEMs versus ϕ_{smooth}: Fig. 13 shows that BEMs provide greater discrimination than simply using ϕ_{smooth}. The normalized values of ϕ_{smooth} for the patches in Fig. 13(a) and (b) are 1 and 1.03, respectively, in the same direction. On the other hand, the normalized BEM values are 5.29 for the former and 1 for the latter. The greater discrimination is apparent in the case of BEMs. Normalized values are used due to the different scales of ϕ_{smooth} and BEMs.

3) Using PBM for **BE** *Selection:* Fig. 14 shows the advantage of BEMs in images with little perceptible motion blur. The image in this figure has a PBM value of 6.73 which is below our threshold τ of 10 and hence, using BEMs should result in an improved segmentation. Note that the motion blur magnitude in the image is small, since the plane is the object focused on and the sky is fairly uniform and hence, does not appear blurred to a large extent. Fig. 14(b) and (c) shows the segmentation results based on motion blur estimates and BEMs, respectively. It can be seen that the plane is segmented well from the sky in Fig. 14(c), demonstrating the efficacy of BEMs.

The need for using a PBM in order to activate the use of BEMs is shown in Fig. 15. The image in this figure has a consistent motion blur and a PBM value of 20.2. It can be seen that using

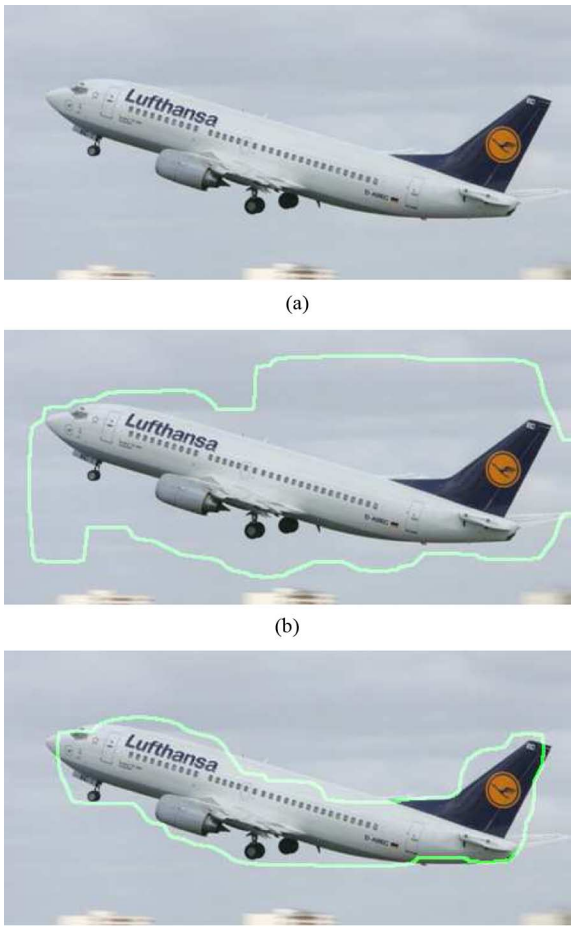

Fig. 14. Segmenting regions with different blur. (a) Image with inconsistent motion blur. (b) Segmentation using motion blur estimates. (c) Segmentation using BEMs.

Fig. 15. Segmenting an image with consistent blur. (a) Image. (b) Segmentation using BEMs. (c) Segmentation using motion blur estimates.

BEMs does not provide a result as good as using motion blurs only for images with significant blurring.

4) Distinguishing Consistent and Inconsistent Regions: Fig. 16 shows how subimages with consistent and inconsistent motion blurs are represented by our method. The consistent subimage has all the pixels belonging to the same region. In general, most of the pixels are classified as belonging to the same region, though some insignificant outliers may be present. In the inconsistent subimages, the segmentation shows distinct separate regions of pixels that indicate the inconsistent regions.

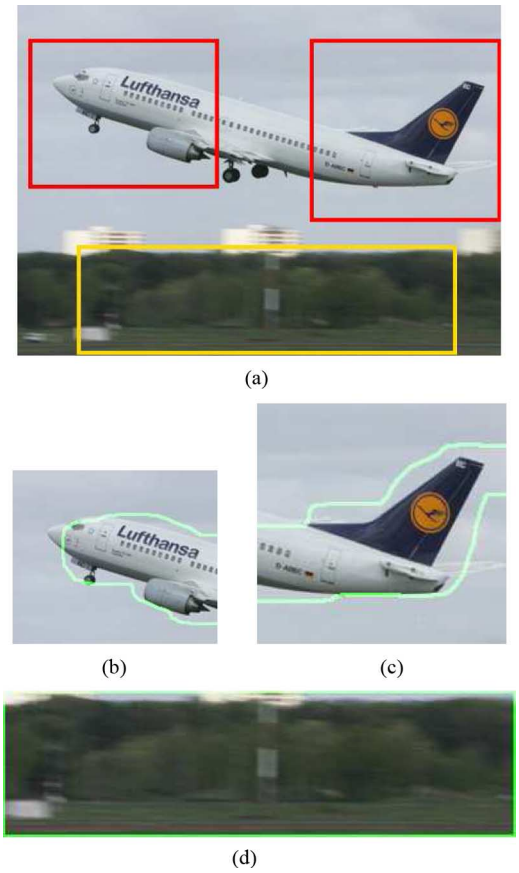

Fig. 16. Distinguishing consistent and inconsistent regions. (a) Red box in image indicates inconsistent region; yellow box indicates consistent region. (b) and (c) Inconsistent region detection. (d) Consistent region detection.

C. Comparisons

There are a few methods that detect image tampering based on different blurs. The work in [9], [14], and [15] used defocus blur modeled with a two-dimensional circular Gaussian kernel. As these methods are based on this isotropic kernel, they cannot be extended directly to directional motion blur. Moreover, all of these methods require considerable human intervention in defining parameters and interpreting results. In another work [16], the authors proposed a method intended for highly localized blur and mentioned that it is not suitable for motion blur. In yet another work [13], the authors suggested that it is possible to distinguish natural and artificial motion blur using their method. So, we compare our method with [13].

The authors of [13] use discrepancies in defocus blur to detect forgeries. We implemented their technique and compared the results of our technique with those obtained using their technique. The technique in [13] is based on normalizing the DCT coefficients of 8×8 image blocks and then computing the inverse DCT of the image. This technique offers the advantages of speed and simplicity. Enhancements such as threshold selection based on global blur estimates and morphological operations may also be used in order to improve the results of the technique. The output images for the best thresholds are shown in Fig. 17. As can be seen, while our technique generates a blob that covers the region with inconsistent blur, the method in [13] results in

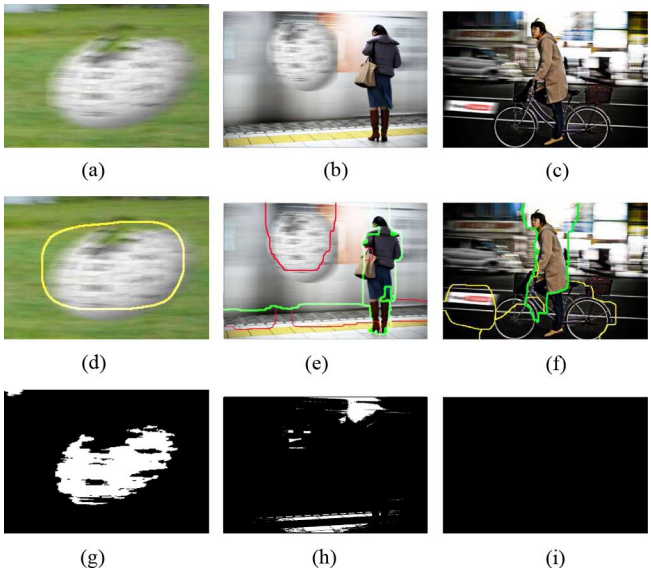

Fig. 17. Comparison with [13]. (a) Image with spliced motion-blurred logo. (b) and (c) Image with multiple motion blurs. (d)–(f) Our results. (g)–(i) Results from [13].

TABLE III
COMPARISON OF SEGMENTATION COSTS

Method	Cost
Proposed energy-based segmentation technique	0.7402×10^{-3}
Proposed Otsu's-method based technique	0.9137×10^{-3}
[13] with blur-adaptive threshold variation	0.9422×10^{-3}

only certain parts of the inconsistent region being identified as inconsistent.

Table III shows the performance of the DCT-based technique for various threshold choices. The average segmentation cost for this technique is calculated on the same database used to obtain Tables I and II. The segmentation cost for selecting a threshold based on a global blur estimate, as in [13], is significantly higher than that obtainable by our method. Although our proposed technique based on Otsu's method offers only slightly better performance than that offered by the DCT-based technique, applying energy-based segmentation gives a significant improvement.

The DCT-based technique is strongly influenced by the color and/or texture of the region with inconsistent motion blur compared to the rest of the image. For example, the image in Fig. 17(g) shows a distinct resemblance to Fig. 17(a) in terms of shading. This indicates a strong dependence on texture in the method of analysis used. Our method usually generates a large blob which allows easy interpretation of results. For images with multiple blurs as in Fig. 17(b) and (c), we are able to segment regions with inconsistent motion blurs. The technique of [13] is not able to do so.

V. CONCLUSIONS

We have presented a technique for detecting spliced images using discrepancies in motion blur in this paper. Motion blur is observed in images of fast-moving subjects and may also appear due to camera shake. We have used the fact that introducing motion blur into a spliced object, in general, depends on the perception of the person creating the forgery and hence, is unlikely to be completely consistent with the blur in the rest of the image.

Our approach has been based on the method of spectral analysis of image gradients. The image gradients of a blurred image in the spectral domain display some periodic characteristics which are correlated with the amount and direction of motion blur present.

The suspected image is divided into overlapping blocks and the motion blur for each block is estimated. This is followed by a postprocessing step of smoothing the blur estimates and upsampling to the size of the image. The regions of the image which show inconsistent blur are then segmented from the image and displayed to the user. We have also developed a BEM to provide robust segmentation, in the case of little perceptible blur. The presence of low blur is determined by using a perceptual blur metric.

We have provided some results of detecting inconsistent regions by using our technique and have compared it with another technique applicable to motion blur. Quantitative and qualitative comparisons show that our technique provides better results in selecting the regions with inconsistent blur.

REFERENCES

[1] Museum of Hoaxes. [Online]. Available: http://www.museumofhoaxes.com/hoax/photo_database/image/tourist_guy/.
[2] B. Mahdian and S. Saic, "A bibliography on blind methods for identifying image forgery," *Image Commun.*, vol. 25, no. 6, pp. 389–399, 2010.
[3] A. Popescu and H. Farid, "Exposing digital forgeries by detecting traces of resampling," *IEEE Trans. Signal Process.*, vol. 53, no. 2, pp. 758–767, Feb. 2005.
[4] H. Farid, Detecting Digital Forgeries Using Bispectral Analysis, Massachusetts Inst. Technol., Cambridge, MA, 1999, Tech. Rep. AIM-1657.
[5] M. Johnson and H. Farid, "Exposing digital forgeries by detecting inconsistencies in lighting," in *Proc. 7th Workshop Multimedia and Security*, 2005, pp. 1–10.
[6] M. Johnson and H. Farid, "Exposing digital forgeries in complex lighting environments," *IEEE Trans. Inf. Forensics Security*, vol. 2, no. 3, pt. 1, pp. 450–461, Sep. 2007.
[7] M. Johnson and H. Farid, "Exposing digital forgeries through chromatic aberration," in *Proc. 8th Workshop Multimedia and Security*, 2006, pp. 48–55.
[8] M. Johnson and H. Farid, Metric Measurements on a Plane From a Single Image, Dept. Comput. Sci., Dartmouth College, 2006, Tech. Rep. TR2006-579.
[9] G. Cao, Y. Zhao, and R. Ni, "Edge-based blur metric for tamper detection," *J. Inf. Hiding Multimedia Signal Process.*, vol. 2073, p. 4212, 2009.
[10] B. Mahdian and S. Saic, "Detection of copy-move forgery using a method based on blur moment invariants," *Forensic Sci. Int.*, vol. 171, no. 2–3, pp. 180–189, 2007.
[11] Y. Yun, J. Lee, D. Jung, D. Har, and J. Choi, "Detection of digital forgeries using an image interpolation from digital images," in *Proc. IEEE Int. Symp. Consumer Electronics*, 2008, pp. 1–4.
[12] S. Bayram, H. Sencar, and N. Memon, "An efficient and robust method for detecting copy-move forgery," in *Proc. IEEE Int. Conf. Acoustics, Speech and Signal Processing*, 2009, pp. 1053–1056.
[13] D. Hsiao and S. Pei, "Detecting digital tampering by blur estimation," in *Proc. 1st IEEE Int. Workshop Systematic Approaches to Digital Forensic Engineering*, 2005, pp. 264–278.
[14] X. Wang, B. Xuan, and S. Peng, "Digital image forgery detection based on the consistency of defocus blur," in *Proc. Int. Conf. Intelligent Information Hiding and Multimedia Signal Processing*, 2008, pp. 192–195.
[15] L. Zhou, D. Wang, Y. Guo, and J. Zhang, "Blur detection of digital forgery using mathematical morphology," *Lecture Notes Comput. Sci.*, vol. 4496, pp. 990–998, 2007.

[16] J. Zhang and Y. Su, "Detecting logo-removal forgery by inconsistencies of blur," in *Proc. Int. Conf. Industrial Mechatronics and Automation*, 2009, pp. 1–4.
[17] P. Kakar, N. Sudha, and W. Ser, "Detecting digital image forgeries through inconsistent motion blur," in *Proc. IEEE Int. Conf. Multimedia & Expo*, 2010, pp. 486–491.
[18] A. Rav-Acha and S. Peleg, "Two motion-blurred images are better than one," *Pattern Recognit. Lett.*, vol. 26, no. 3, pp. 311–318, 2005.
[19] X. Liu and A. G. El, "Simultaneous image formation and motion blur restoration via multiple capture," in *Proc. IEEE Int. Conf. Acoustics Speech And Signal Processing*, 2001, vol. 3, pp. 1841–1844.
[20] D. Gennery, "Determination of optical transfer function by inspection of frequency-domain plot," *J. Opt. Soc. Amer. (1917–1983)*, vol. 63, p. 1571, 1973.
[21] M. Cannon, "Blind deconvolution of spatially invariant image blurs with phase," *IEEE Trans. Acoust., Speech, Signal Process.*, vol. 24, no. 1, pp. 58–63, Feb. 1976.
[22] I. Rekleitis, "Steerable filters and cepstral analysis for optical flow calculation from a single blurred image," *Vis. Interface*, vol. 1, pp. 159–166, 1996.
[23] H. Ji and C. Liu, "Motion blur identification from image gradients," in *Proc. IEEE Conf. Computer Vision and Pattern Recognition*, 2008, pp. 1–8.
[24] S. Dai and Y. Wu, "Motion from blur," in *Proc. IEEE Conf. Computer Vision and Pattern Recognition*, 2008, pp. 1–8.
[25] S. Geman and D. Geman, "Stochastic relaxation, Gibbs distributions and the Bayesian restoration of images," *IEEE Trans. Pattern Anal. Mach. Intell.*, vol. 6, no. 6, pp. 721–741, Nov. 1984.
[26] P. Marziliano, F. Dufaux, S. Winkler, and T. Ebrahimi, "A no-reference perceptual blur metric," in *Proc. IEEE Int. Conf. Image Processing*, Citeseer, 2002, vol. 3, pp. 57–60.
[27] N. Otsu, "A threshold selection method from gray-level histograms," *Automatica*, vol. 11, pp. 285–296, 1975.
[28] Y. Boykov, O. Veksler, and R. Zabih, "Fast approximate energy minimization via graph cuts," *IEEE Trans. Pattern Anal. Mach. Intell.*, vol. 23, no. 11, pp. 1222–1239, Nov. 2002.
[29] A. Levin, A. Rav-Acha, and D. Lischinski, "Spectral matting," in *Proc. IEEE Conf. Computer Vision and Pattern Recognition*, 2007, pp. 1–8.
[30] Flickr. [Online]. Available: http://www.flickr.com.
[31] D. Huttenlocher, G. Klanderman, and W. Rucklidge, "Comparing images using the Hausdorff distance," *IEEE Trans. Pattern Anal. Mach. Intell.*, vol. 15, no. 9, pp. 850–863, Sep. 1993.
[32] X. Yu, M. Leung, and Y. Gao, "Hausdorff distance for shape matching," in *Proc. 4th IASTED Int. Conf. Visualization, Image and Image Processing*, 2004.
[33] M.-P. Dubuisson and A. Jain, "A modified Hausdorff distance for object matching," in *Proc. IAPR Int. Conf. Computer Vision Image Processing*, Oct. 1994, pp. 566–568.

Pravin Kakar (S'10) received the B.Tech. degree in electronics engineering from the Veermata Jijabai Technological Institute, Mumbai, India, in 2009. He is currently pursuing the Ph.D. degree at the Institute for Media Innovation, Nanyang Technological University, Singapore.

His research interests include image forensics, multimedia signal processing, and computer vision.

N. Sudha (M'99–SM'07) received the B.E degree from Madurai Kamaraj University, Madurai, India, in 1992, the M.S. degree from the Indian Institute of Technology (IIT) Madras, Chennai, India, in 1997, and the Ph.D. degree from IIT Guwahati, Guwahati, India, in 2001.

She has been working as an Assistant Professor in the School of Computer Engineering, Nanyang Technological University, Singapore, since 2006. Previously, she was employed at IIT Madras and IIT Guwahati. She has published around 60 papers in refereed international journals and conferences. She is the principal investigator of three funded research projects. Her research areas include machine vision and image processing, VLSI architecture design, and neural networks.

Dr. Sudha is on the editorial board of a few international journals. She also served as program committee member and chaired a few sessions in international conferences.

Wee Ser (M'83–SM'97) received the Ph.D. degree in electrical and electronic engineering in 1982.

He joined the Defence Science Organization (DSO) in 1982 and became Head of the Communications Research Division in 1993. In 1996, he was appointed the Technological Advisor to the CEO of the DSO National Laboratories. In 1997, he joined the Nanyang Technological University, Singapore, and has since been appointed Director for the Centre for Signal Processing. He has published more than 130 research papers in refereed international journals and conferences. He holds six patents and is a co-author of six book chapters. He is the Principal Investigator of several externally funded research projects. His research interests include sensor array signal processing, signal detection and classification, channel estimation and equalization, and media signal processing.

Dr. Ser is currently an IEEE Distinguished Lecturer and an Associate Editor for *IEEE Communications Letters* and *Journal of Multidimensional Systems and Signal Processing* (Springer). He is a member of a TC in the IEEE Circuit and System Society. He was a recipient of the Colombo Plan scholarship and the PSC postgraduate scholarship. He was awarded the IEE Prize during his studies in the U.K. While in DSO, he was a recipient of the prestigious Defence Technology Prize (Individual) 1991 and the DSO Excellent Award 1992.